Selective CO_2 Electrocatalysis at the Pseudocapacitive Nanoparticle/Ordered-Ligand Interlayer

Authors: Dohyung Kim[1,2,3,†], Sunmoon Yu[1,3,†], Fan Zheng[4], Yifan Li[2,3], Sheena Louisia[2,3], Heinz Frei[5], Lin-Wang Wang[4], and Peidong Yang[1,2,3,6]*

Affiliations:

[1]Department of Materials Science and Engineering, University of California, Berkeley, CA 94720, USA.

[2]Department of Chemistry, University of California, Berkeley, CA 94720, USA.

[3]Chemical Sciences Division, Lawrence Berkeley National Laboratory, Berkeley, CA 94720, USA.

[4]Joint Center for Artificial Photosynthesis and Materials Science Division, Lawrence Berkeley National Laboratory, Berkeley, CA 94720, USA.

[5]Molecular Biophysics and Integrated Bioimaging Division, Lawrence Berkeley National Laboratory, CA 94720, USA.

[6]Kavli Energy NanoScience Institute, Berkeley, CA 94720, USA.

*Correspondence to: p_yang@berkeley.edu

†These authors have contributed equally.

(*Nature Energy*, accepted)

Abstract:

Enzymes distinctively feature concerted operation of multiple components around an active site, leading to exquisite specificity. Realizing such configurations on synthetic catalyst surfaces remains elusive. Here, we report the creation of a Nanoparticle/Ordered-Ligand Interlayer (NOLI) that contains a multi-component catalytic pocket for high-specificity CO_2 electrocatalysis. Through the collective behavior of ligands, the NOLI contains a detached ligand layer remaining within the metal surface vicinity. The interlayer possesses unique pseudocapacitive characteristics where desolvated cations are interposed and the resultant active site configuration enhances catalytic turnover by two orders of magnitude. The generality of the NOLI design is demonstrated across a number of transition metals, ultimately achieving up to 99% selectivity towards CO at marginal overpotentials, with onset overpotentials of as low as 27 mV.

One Sentence Summary:

An unprecedented catalytic machinery composed of metal nanoparticles with a floating layer of ligands is found to enable selective CO_2 catalysis.

Main text:

Among the vast amount of efforts in heterogeneous catalysis (*1, 2*), one particular direction that has received continued interest is the creation of catalytic machineries that are structurally/functionally equivalent to enzymes. Enzymes achieve superior catalytic specificity and high turnover by creating optimal nanoscale environments around active sites using amino acid side chains, in which molecular recognition and subsequent catalysis are synergistically conducted (*3, 4*). Mimicking the mechanism by which enzymes operate demands a transition to a more holistic perspective of a catalyst that critically considers the interplay between a metal site and its surrounding molecular environment.

To this end, the strategy largely employed has been functionalization of metal surfaces (*e.g.* nanoparticles) using tethered ligands, which contain moieties affecting active sites and/or reactant intermediates (*5-12*). The tethered-ligand strategy has been explored with catalysts for thermochemical (*5, 6*) and electrochemical reactions (*7-12*), especially within electrocatalysts that pursue the exquisite selectivity of their enzyme equivalents for reactions such as the two-electron reduction of CO_2 to CO/formate (*13, 14*). Creating such sophisticated ideal catalysts requires the precise configuration of multiple functional groups and mobile parts that dynamically respond to external stimuli. The structural complexity of such synthetic constructs has made their creation challenging, thereby limiting the catalytic performance of current strategies. Moreover, such efforts for electrocatalysis should further consider any possible interactions between the synthetic catalyst and components of an electrochemical interface (*i.e.* solvated electrolyte ions and solvent

molecules), which have been previously overlooked. Therefore, a synthetic electrocatalyst functioning through cooperatively combining all of the above aspects has yet been developed.

In this work, we report a new class of nanoparticle catalyst which contains a unique interlayer structure between the nanoparticle surface and a floating layer of ligands at which electrocatalysis is promoted (Fig. 1). This so-called Nanoparticle/Ordered-Ligand Interlayer (NOLI) is created by the collective dissociation of bound ligands from a dense assembly of nanoparticles (NPs) when biased, forming an ordered ligand layer at their vicinity yet without complete loss into the solution. The resulting NOLI is pseudocapacitive through desolvated electrolyte cations; this unique interfacial configuration, composed of metal atoms and a vicinal anionic ligand layer associating desolvated cations, provides a catalytic hotspot for selective CO_2 transformation. The modularity of the structure is presented over a number of metal NPs (M-NOLI catalysts) with various electrochemical environments that resulted in orders of magnitude enhancement in turnover and nearly unit selectivity (~99%) for CO_2-to-CO.

The NOLI forms by using colloidal metal NPs and for Ag-NOLI, Ag NPs synthesized with tetradecylphosphonic acid (TDPA) ligands are used as a precursor (Fig. S1). X-ray photoelectron spectroscopy (XPS) shows that the phosphonic head group of the TDPA ligand binds to the Ag NP surface through two oxygen atoms in a bidentate mode (Fig. 1 and Fig. S2-4). To initiate Ag-NOLI formation, Ag NPs are assembled on a carbon paper support with the NPs interfacing each other in an array (Fig. 2A and S5). In this specific configuration, application of bias by a potential sweep results in a cathodic peak from the passage of reductive charge (Fig. 2B) owing to the dissociation of chemisorbed (*i.e.* covalently bonded) surface ligands (hereafter,

dissociation refers to reductive cleavage of covalent bonds and desorption refers to desorption of adsorbed, that is physisorbed, ligands). The peak observed does not exist for Ag foil, excluding the possibility of its being an inherent characteristic of Ag (Fig. S6). The reductive charge (C) of the peak estimates all of the NP ligands to be dissociated (Supplementary Text). This is well characterized in the O 1*s* spectrum (Fig. 2C) after the potential sweep, showing the loss of P-O-Ag bonds and a transition to a physisorbed state for the phosphonic oxygens (P=O/P-O). Accordingly, the P 2*p* signal located at 132.4 eV, due to the formation of P-O-Ag bonds, shifts to 133.7 eV from their loss (Fig. 2D).

However, the ligands lifted from the NP surface by the application of bias are never fully removed. A cyclic voltammetry (CV) scan after the first reductive sweep of assembled Ag NPs exhibits a reversible ad/desorption feature (Fig. 2E), which is again absent for Ag foil (Fig. S6). We attribute this feature to the reversible adsorption of ligands on the Ag NPs (Fig. 1), similar to phosphate anion ad/desorption on a silver surface (*15*). A stable CV response during multiple scans (Fig. 2F) indicates that the desorbed ligands under negative biases remain in the vicinity of NP surfaces rather than being completely lost into the solution, a unique feature of the NOLI.

Furthermore, assembly of NPs is a precondition to this collective dissociation of ligands by the application of bias. When individual NPs are isolated on the carbon support, both the cathodic peak during the initial potential sweep and the reversible ad/desorption features of the dissociated ligands are not present (Fig. S6). For the NPs in an isolated configuration, the ligands remain covalently attached and do not transit to the reversible physisorption state, as will be discussed more in detail below. Overall, we find that the close assembly of NPs triggers the NOLI

formation by allowing intimate interactions between ligand chains of a large number of NPs.

Not only is the collective behavior of ligands responsible for their initial dissociation, but it should be critical for allowing the ligand layer to remain stable near the NP surface despite being at a desorbed state under negative biases (*16*). Among efforts to understand the structure of the ligand shell on metal NPs (*17*), one particular way to probe its degree of structural order is to look at the CH_2 stretching vibrations (ν_{as} and ν_s), where increased disorder results in a shift to higher wavenumbers (*6, 18-20*). The infrared (IR) spectrum of Ag-NOLI formed indicates a structurally ordered ligand layer (Fig. 2G), based on the CH_2 stretching frequencies ($\nu_{as}(CH_2)$: 2917.1 cm^{-1}, $\nu_s(CH_2)$: 2849.8 cm^{-1}) that align closely with those of TDPA crystals (Fig. S7). The dense assembly of NPs is expected to promote interactions between the ligand chains to allow this transition to a more ordered configuration (Fig. S7) (*16, 19*). Therefore, the NOLI formation (Fig. 1) can be described as a collective dissociation of ligands from assemblies of NPs when electrically biased, leading to a structurally ordered ligand layer stabilized by the non-covalent interactions between dense alkyl chains with dynamic responses to biases.

Given the reversible ad/desorption of the ligand layer in the NOLI structure, an interlayer exists at negative biases between the NP surface and the desorbed ligand layer in its vicinity (Fig. 1). We find that this region can act as a catalytic pocket for promoting CO_2 conversion. Once the ligand layer desorbs at negative biases, rise in currents due to electrochemical reduction of CO_2 can be observed (Fig. 2E). When applying a stationary bias (Fig. S8), a stable current response is recorded and Ag-NOLI is able to promote selective CO formation in contrast to the H_2-selective activity observed on a pristine Ag foil (Fig. 2H). Specific activity of Ag-NOLI towards CO,

taking into account its electrochemically accessible surface area, is approximately two orders of magnitude higher than that of the Ag foil (Fig. 2H and S8). In contrast, a more typical arrangement of isolated Ag NPs (Fig. S6) only results in a minor increase in the CO_2 reduction activity (Fig. S8), supporting the unique catalytic role of the NOLI structure. Although the conditions required to create Ag-NOLI results in larger particles, its size cannot account for the high CO turnover as the structure should be reaching closer to the bulk polycrystalline limit (Fig. S9). Furthermore, the particles grow from 6 to 32 nm during electrolysis without a change of CO FE, lending little credibility to the idea that NP size is a catalytic descriptor for the improvement observed (Fig. S9). Similarly, the crystallites continuously grow throughout, further eliminating any correlation between crystallite size and catalytic activity (Fig. S9). However, when the ligand layer is intentionally removed from Ag-NOLI, the CO FE and turnover drop to levels similar to Ag foil (Fig. 2H and S10), strongly supporting the catalytic role of NOLI for the selective CO_2-to-CO transformation that is further evidenced by the 97% CO selectivity as high as 97% obtained by Ag-NOLI (Fig. S11).

Importantly, after the early loss of ligands that coincides with vast rearrangement of catalysts by NP coalescence and fusion (Fig. S9), the ligand density (with respect to the NP surface area) remains relatively stable throughout electrolysis though at a desorbed state (Fig. 2I). Characterizations by CV and XPS indicate that the NOLI structure remains stable during its catalytic promotion for CO_2 conversion (Fig. S12). In contrast, when Ag NPs are isolated, the ligands either remain covalently bonded or are entirely lost to the surrounding environment, both typical situations expected for ligand-capped nanoparticles. Tracking the isolated Ag NPs throughout reduction shows that surface ligands remain covalently attached in their original

bonding configuration, while some portion is gradually lost to the solution leading to an increase in their structural disorder (Fig. S13 and S14). Moreover, the remaining surface density of ligands is lower for the isolated NPs even though the ligand layer for the NOLI operates at a desorbed state, likely due to absence of stabilizing interactions between ligands. All these observations highlight the unconventional structural state for the NP catalyst under bias and an unprecedented role for ligands in the NOLI structure.

Despite the growing awareness of the role of the electrochemical interface and its constituents for catalytic reactions (*21-27*), tethered-molecule functionalization approaches generally do not consider their presence and effects, limiting our understanding and manipulation of electrochemical reactions at heterogenous surfaces (*7-12*). In order to probe the interplay between the NOLI and electrochemical environment, several techniques are employed. First, electrochemical impedance spectroscopy (EIS) is used at the catalytically relevant conditions. Figure 3A shows the Bode plot of Ag-NOLI at -0.68 V vs. RHE. By comparing with the simulated Bode plots of a typical heterogeneous electrocatalytic interface, we observe that Ag-NOLI exhibits not only a low charge transfer resistance for CO_2 conversion, but a surprisingly high capacitance (Fig. S15). Furthermore, in the Nyquist plots (Fig. 3B and S16), we find a characteristic feature (a smaller semicircle in the high frequency region) indicative of a pseudocapacitive interface in parallel with charge transfer resistance and double layer capacitance, which is absent in the other systems. With the EIS data at various potentials fitted (equivalent circuit in Fig. 3B), pseudocapacitance values associated with Ag-NOLI could be extracted (Fig. S17 and Table S1). The specific capacitance of Ag-NOLI (Fig. 3C) is estimated to be about six times higher than that of the Ag foil, which is at typical values (30 – 40 $\mu F/cm^2$) for

metals in alkali metal-based electrolytes (*28*). When the NOLI is removed, these values decrease back to similar levels to Ag foil together with the loss of the pseudocapacitive characteristic as observed from EIS (Fig. 3C and S18). Accordingly, not only do the reversible ad/desorption features of the ligand layer disappear, but there is a significant collapse of the capacitive charge stored after the NOLI removal (Fig. 3D) (*29*). Therefore, we actually find that Ag-NOLI exhibits pseudocapacitance, which has been observed for metal derivatives (*i.e.* transition metal oxides, TMDC, and MXene) but not for pure metals so far (*30, 31*). Furthermore, its unique presence should have an influence on promoting the electrocatalytic conversion of CO_2.

Considering the pseudocapacitive behavior of metal derivatives (*29-31*), we expect its origin in the NOLI structure to be cation insertion/adsorption at the interlayer region between the NP surface and ligand layer (Fig. 3E). It is also interesting to note that the NOLI represents a heterostructured metal-organic interlayer for ion/charge storage, a first of the kind. The presence of associated dehydrated cations can be probed by X-ray absorption near edge structure (XANES), since the potassium *K*-edge is sensitive to its surrounding coordination environment. Potassium ions hydrated in aqueous solutions exhibit a symmetric single absorption peak (3616.5 eV), in contrast to potassium salts that feature a white line splitting caused by the asymmetry of the surrounding electric field due to pairing of the counter anions (Fig. S19) (*32, 33*). K XANES of Ag-NOLI (sealed with electrolyte during electrolysis) exhibits features distinct from the spectra of the Ag foil and the carbon paper used as a support, both of which present hydrated K^+ (Fig. 3F). Specifically, a main absorption peak at 3617.8 eV with a shoulder at 3614.0 eV is observed indicating the presence of dehydrated K^+. Notably, the dehydrated K^+ signature is detected even with a large amount of liquid layer containing hydrated K^+ on top of the electrode,

suggesting a significant presence of dehydrated potassium ions. Molecular dynamics (MD) simulation on a model structure mimicking Ag-NOLI further confirms the presence of dehydrated K^+. In contrast to a K^+ ion at the outer Helmholtz plane (3.9 Å) of a bare silver surface (*26*), the radial distribution function (RDF) of water-oxygen atoms around K^+ exhibits a significant reduction, mainly at the first peak around 2.8 Å representing the first layer of water molecules (Fig. 3G) (*34*). It also seems that the interaction of K^+ to the phosphonic head group of ligands drives its conditions in the NOLI structure (Fig. S20). In addition, K 2*p* XPS indicates a larger presence of K^+ that should be associated with the NOLI (Fig. S21). Therefore, we posit that the NOLI encompasses dehydrated cations at the interlayer by its interactions with the electrochemical environment.

The structural details of Ag-NOLI present a unique reaction center for CO_2 catalysis that is composed of a metal atom and dehydrated K^+ held by the vicinal phosphonate ligand. It is suited for stabilizing molecules through electrostatic interactions by the close operation of both ends of the negatively charged metal site and unshielded K^+, which should be necessary for CO_2 activation (Fig. 3H). The polarization of a non-polar CO_2 with an electron transfer to form a $*CO_2^{\bullet-}$ is often considered the energetically demanding step (*35*) as supported by a deuterated solvent experiment (Fig. S22). Through free energy calculations using the explicit solvent models obtained in the MD simulations, we find that the specific reaction center configuration for the NOLI can facilitate the bending of the adsorbed CO_2 molecule (*i.e.* b-$CO_2^{\delta-}$, chemisorbed CO_2) often considered necessary (Fig. 3H and S22) to transit to $*CO_2^{\bullet-}$. In contrast, for a typical electrochemical interface with hydrated K^+ at the OHP, formation of b-$CO_2^{\delta-}$ requires overcoming a large energy barrier.

Considering the structure identified and catalytic mechanism revealed, the principle of operation involving the NOLI contains interesting aspects resembling an enzyme. Not only is the reaction center composed of multiple components, but they are pre-organized/-positioned with the right elements so that a strong electrostatic interaction could stabilize a key intermediate state, a previously established mechanism for enzymatic catalysis (*4*). It is also the specific site arrangement that disfavors undesired catalytic pathways, *e.g.* hydrogen evolution. Furthermore, the entire structure is stabilized by the interactions of the hydrocarbon chains at the ligand layer, which is similar to the role of interactions between amino acid side chains for proteins that hold their structure. In addition, the NOLI keeps a constant active-site environment by minimizing the impact from external chemical conditions. Whereas an increase in bicarbonate concentration typically leads to lower selectivity (*i.e.* higher H_2 FE) due to the increase in the hydrogen donor concentration (Fig. S24A), Ag-NOLI retains its high CO FE (Fig. 3I). Rather, the structural stability of the ligand layer seems reinforced by the increase in buffer strength, limiting dissolution of the phosphonic head group containing ligands (Fig. S24B) (*36*).

From an interfacial perspective, the NOLI-based catalysis demonstrates manipulation of near-surface regions of the electrochemical double layer by a metal-organic heterostructure. With recent focus to the fundamental roles of electrolyte ions and solvents for electrochemical reactions (*24, 26, 27, 37*), it is important to develop materials that can modulate the electrochemical interface structure favorable for catalysis. For instance, despite their role suggested for stabilizing CO_2 reduction intermediates (*26, 27, 37*), hydrated cations at the interface pose limited effects as observed from the catalytic activity of polycrystalline Ag foil (Fig. 2H). Consequently, smaller alkali cations (*e.g.* Li^+) with large hydration energy (Fig. S25)

and tightly bound solvation shell exhibit negligible effects leading to worse catalytic behavior. However, such cations recover their utility when dehydrated and organized at the NOLI`s reaction center. For example, Ag-NOLI in 0.1 M $LiHCO_3$ is able to attain near 70% CO FE in contrast to the 3% obtained from the Ag foil (Fig. 3I), on which even further bias to negative potentials only allows ~35% at maximum.

To extend the idea that M-NOLI is a modular structure that synergistically promotes catalysis, we explored the translation of NOLI to other noble metal-based NPs (Au- and Pd-NOLI). Among the transition metals, gold and palladium have been known for their favorable characteristics in CO_2 conversion (*2, 38*). Au-NOLI based on Au NPs with identical ligand chemistry (Fig. S26) attains highly selective CO formation (98.9%) with its structure confirmed similarly as with Ag-NOLI (Fig. S27). In addition, Au-NOLI achieves high selectivity in various cationic environments (*i.e.* Li^+, K^+, and Cs^+); however, interestingly, the potential at which the system catalytically operates tends to be cation-dependent (Fig. S28). Small cations such as Li^+ requires more negative biases to be introduced into the NOLI presumably due to their larger hydration energies and thus tightly bound solvation shells, which consequently affects the wettability of the system and accessibility of Au-NOLI to the surrounding environment (Fig. S28). Meanwhile, Au-NOLI in a Cs^+-based environment shows a minimal onset overpotential (27 mV), furthermore approaching nearly unit selectivity (98.5%) at -0.36 V vs. RHE with little effect from the bulk electrolyte concentration (Fig. 4A). Specific activity is enhanced around two orders of magnitude as well (Fig. 4B). Moreover, the catalyst can operate in the long-term (Fig S29A) and removal of the NOLI results in significant drop of CO FE (Fig. S29B). The superior selectivity of Au-NOLI stands out against previously reported Au-based catalysts (Fig. S30).

Similarly, Pd-NOLI also enables selective conversion of CO_2 to formate or CO, depending on the applied potential range (Fig. 4C and S31). Its CO selectivity at low overpotentials (*e.g.* 96.9% at -0.55 V) stands out compared with other Pd-based catalysts (Fig. S32). Overall, through modular design of a metal-NOLI catalyst, a variety of highly selective CO_2 conversions can be achieved.

In conclusion, the NOLI presents a new picture of ligands as part of a functional nanoparticle. It enables creation of a catalytic reaction center, in harmony with the electrochemical environment, that functions through close cooperation of multiple components leading to efficient stabilization of transition states and driving selective catalysis. From such a discovery, we anticipate nanoparticle catalyst design to expand in efforts to create enzymatic counterparts that may bring a range of catalytic reactions closer to ideal. Furthermore, its unique way of ion interactions presents the NOLI as a class of material potentially useful for various other applications such as energy storage.

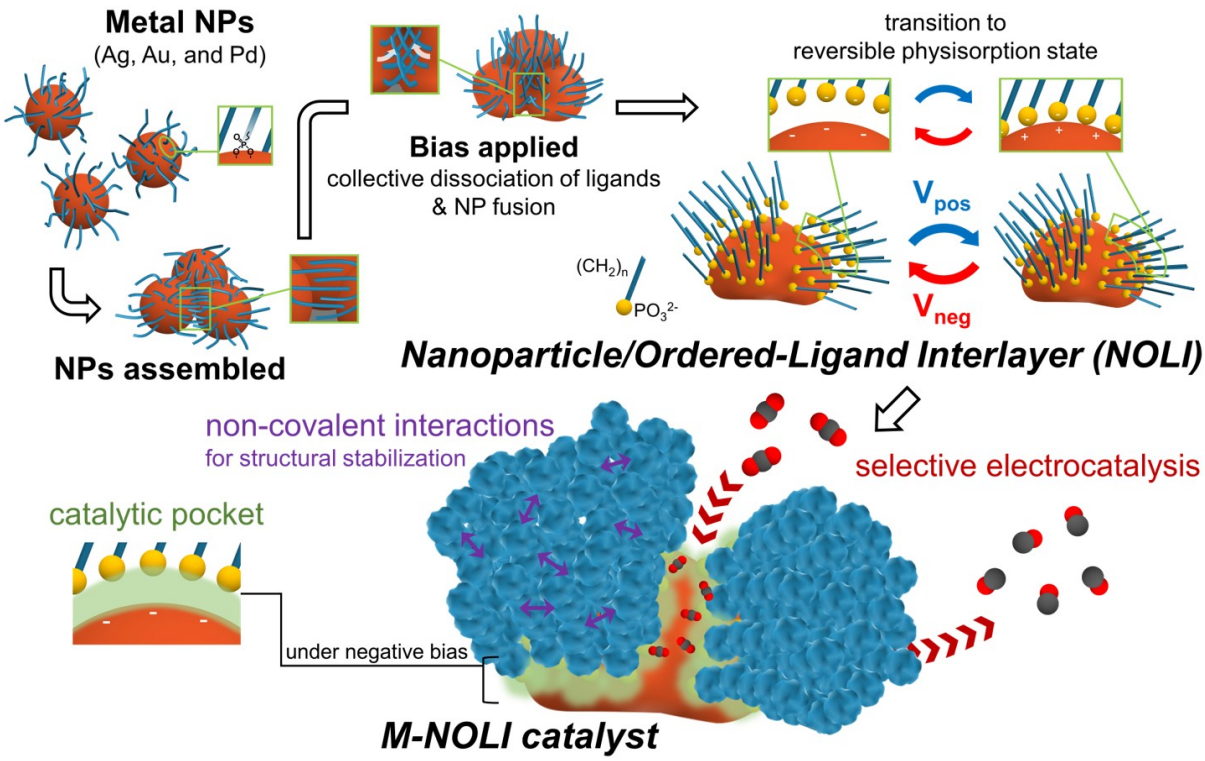

Fig. 1. Schematic illustrating the formation of a Nanoparticle/Ordered-Ligand Interlayer (NOLI) and a metal-NOLI catalyst (M-NOLI) for selective electrocatalysis. Blue chains on the metal NPs represent chemically bonded alkylphosphonic ligands. Upon negative bias on the NPs assembled, the ligands collectively dissociate from the metal surface during NP fusion and transit to a reversible physisorption state (explicitly shown by the yellow phosphonic head group emphasized). The ligand layer maintains its stability through the non-covalent interactions of the alkyl tails (blue) in an ordered configuration. The resultant M-NOLI catalyst provides a unique catalytic pocket for selective CO_2 electroconversion.

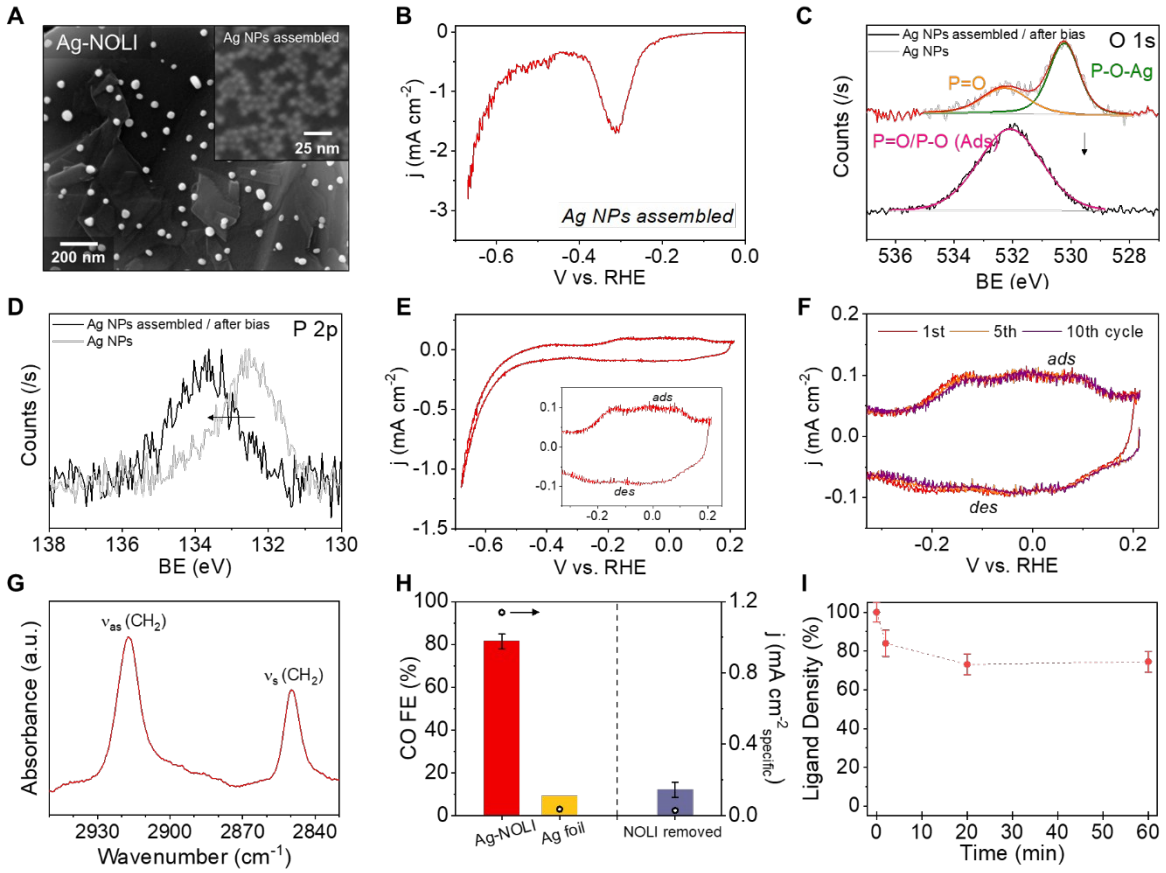

Fig. 2. NOLI formed by the collective dissociation of ligands from an assembly of NPs. (**A**) Scanning electron microscopy (SEM) images of Ag-NOLI and Ag NPs assembled (inset). (**B**) Initial linear sweep voltammetry (LSV) of Ag NPs assembled. (**C**) O 1*s* and (**D**) P 2*p* XPS spectra of Ag NPs assembled before and after being biased. (**E**) Cyclic voltammetry (CV) of Ag-NOLI, after the first LSV of assembled Ag NPs (**B**) that led to collective dissociation of ligands. (**F**) Multiple CV scans of Ag-NOLI. (**G**) IR spectra of Ag-NOLI. (**H**) CO FE and specific current density of Ag-NOLI, Ag foil, and when the NOLI is removed at -0.68 V vs. RHE. Error bars are one standard deviation of three independent measurements. (**I**) Ligand density of Ag-NOLI estimated from XPS throughout CO_2 electrolysis. All electrochemical tests are conducted in 0.1 M $KHCO_3$ at 1 atm CO_2.

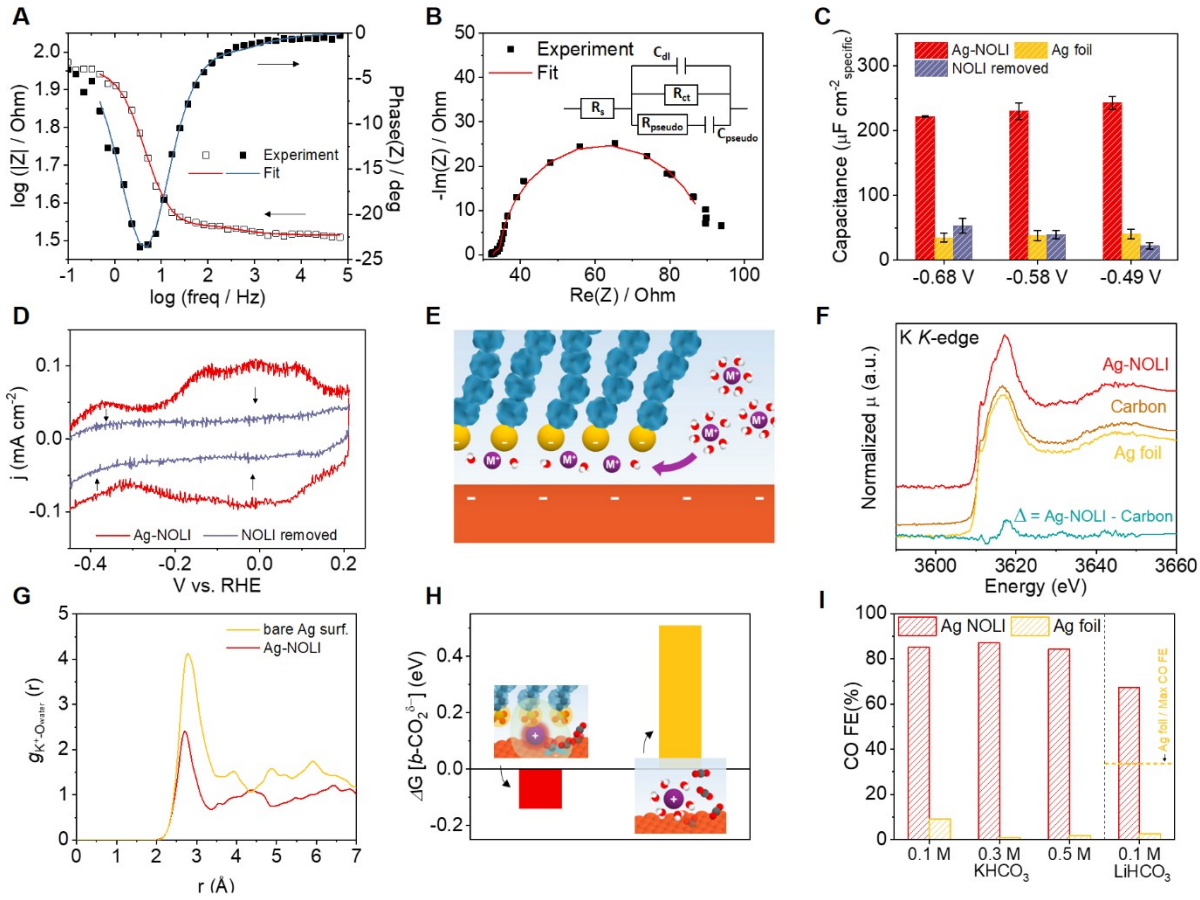

Fig. 3. Pseudocapacitive behavior of the NOLI and its effect on CO_2 catalysis. (**A**) Bode and (**B**) Nyquist plots of Ag-NOLI measured at -0.68 V vs. RHE. Inset in (**B**) shows the equivalent circuit diagram of Ag-NOLI composed of solution resistance (R_s), double layer capacitance (C_{dl}), charge transfer resistance (R_{ct}), pseudocapacitance (C_{pseudo}), and charger transfer resistance for pseudocapacitance (R_{pseudo}) that is used to fit the experimental data for both (A) and (B). (**C**) Specific capacitance measured for Ag-NOLI, Ag foil and NOLI removed. Real surface areas are estimated from Pb underpotential deposition. (**D**) CV of Ag-NOLI and NOLI removed. (**E**) Schematic illustrating the desolvated cation insertion/adsorption at the NOLI (**F**) XANES at the K *K*-edge measured for Ag-NOLI, Ag foil, and carbon paper. (**G**) Radial distribution function of O_{water} from K^+ for the two different structures modeled. (**H**) $\Delta G[b\text{-}CO_2^{\delta-}]$, the free energy

difference from CO_2 physisorbed (linear) to CO_2 chemisorbed (bent), calculated for the two different structures modeled. The values are the average of 5 different solvent fluctuations considered (Fig. S22) for the explicit solvent model used. (**I**) CO FE of Ag-NOLI and Ag foil tested under various concentrations of $KHCO_3$ at -0.68 V (left) and 0.1 M $LiHCO_3$ at -0.94 V (right). Dashed line indicates the maximum CO FE of Ag foil obtained using 0.1 M $LiHCO_3$ at -1.16 V.

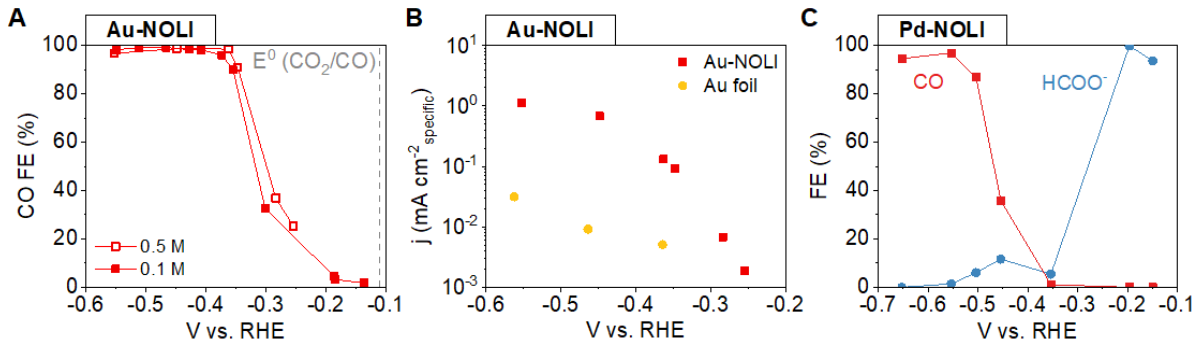

Fig. 4. Au- and Pd-NOLI for selective CO_2 electrocatalysis. (**A**) CO FE of Au-NOLI in $CsHCO_3$ at 1 atm CO_2, showing a minimal onset potential close to the theoretical value for CO production and high selectivity at low overpotentials. Gray dashed line indicates the standard reduction potential of CO_2 to CO. (**B**) Specific CO activity of Au-NOLI and Au foil in 0.5 M $CsHCO_3$ at 1 atm CO_2. (**C**) Electrocatalytic selectivity of Pd-NOLI in 0.5 M $KHCO_3$ at 1 atm CO_2.

References and Notes

1. L. Liu, A. Corma, Metal Catalysts for Heterogeneous Catalysis: From Single Atoms to Nanoclusters and Nanoparticles. *Chem Rev* **118**, 4981-5079 (2018).
2. Z. W. Seh *et al.*, Combining theory and experiment in electrocatalysis: Insights into materials design. *Science* **355**, (2017).
3. D. Ringe, G. A. Petsko, Biochemistry. How enzymes work. *Science* **320**, 1428-1429 (2008).
4. S. D. Fried, S. G. Boxer, Electric Fields and Enzyme Catalysis. *Annu Rev Biochem* **86**, 387-415 (2017).
5. G. Chen *et al.*, Interfacial electronic effects control the reaction selectivity of platinum catalysts. *Nat Mater* **15**, 564-569 (2016).
6. S. T. Marshall *et al.*, Controlled selectivity for palladium catalysts using self-assembled monolayers. *Nat Mater* **9**, 853-858 (2010).
7. B. Genorio *et al.*, Selective catalysts for the hydrogen oxidation and oxygen reduction reactions by patterning of platinum with calix[4]arene molecules. *Nat Mater* **9**, 998-1003 (2010).
8. Y. Zhao, C. Y. Wang, Y. Q. Liu, D. R. MacFarlane, G. G. Wallace, Engineering Surface Amine Modifiers of Ultrasmall Gold Nanoparticles Supported on Reduced Graphene Oxide for Improved Electrochemical CO2 Reduction. *Advanced Energy Materials* **8**, 1801400 (2018).
9. Z. Wang *et al.*, Surface Ligand Promotion of Carbon Dioxide Reduction through Stabilizing Chemisorbed Reactive Intermediates. *J Phys Chem Lett* **9**, 3057-3061 (2018).
10. Z. Cao *et al.*, Tuning Gold Nanoparticles with Chelating Ligands for Highly Efficient Electrocatalytic CO2 Reduction. *Angew Chem Int Ed Engl* **57**, 12675-12679 (2018).
11. Y. Fang, J. C. Flake, Electrochemical Reduction of CO2 at Functionalized Au Electrodes. *J Am Chem Soc* **139**, 3399-3405 (2017).
12. C. Kim *et al.*, Insight into Electrochemical CO2 Reduction on Surface-Molecule-Mediated Ag Nanoparticles. *ACS Catalysis* **7**, 779-785 (2016).
13. F. A. Armstrong, J. Hirst, Reversibility and efficiency in electrocatalytic energy conversion and lessons from enzymes. *Proc Natl Acad Sci U S A* **108**, 14049-14054 (2011).
14. A. Bassegoda, C. Madden, D. W. Wakerley, E. Reisner, J. Hirst, Reversible interconversion of CO2 and formate by a molybdenum-containing formate dehydrogenase. *J Am Chem Soc* **136**, 15473-15476 (2014).
15. C. B. Salim Rosales, M. I. Rojas, L. B. Avalle, Differentiated interactions in phosphate solutions: Comparing Ag(111) and Ag(100) surfaces. *Journal of Electroanalytical Chemistry* **799**, 487-496 (2017).
16. J. D. C. Jacob, T. R. Lee, S. Baldelli, In Situ Vibrational Study of the Reductive Desorption of Alkanethiol Monolayers on Gold by Sum Frequency Generation Spectroscopy. *The Journal of Physical Chemistry C* **118**, 29126-29134 (2014).
17. Q. Ong, Z. Luo, F. Stellacci, Characterization of Ligand Shell for Mixed-Ligand Coated Gold Nanoparticles. *Acc Chem Res* **50**, 1911-1919 (2017).

18. M. D. Porter, T. B. Bright, D. L. Allara, C. E. D. Chidsey, Spontaneously organized molecular assemblies. 4. Structural characterization of n-alkyl thiol monolayers on gold by optical ellipsometry, infrared spectroscopy, and electrochemistry. *Journal of the American Chemical Society* **109**, 3559-3568 (1987).
19. J. C. Love, L. A. Estroff, J. K. Kriebel, R. G. Nuzzo, G. M. Whitesides, Self-Assembled Monolayers of Thiolates on Metals as a Form of Nanotechnology. *Chemical Reviews* **105**, 1103-1170 (2005).
20. R. L. Jones, N. C. Pearsall, J. D. Batteas, Disorder in Alkylsilane Monolayers Assembled on Surfaces with Nanoscopic Curvature. *The Journal of Physical Chemistry C* **113**, 4507-4514 (2009).
21. V. R. Stamenkovic, D. Strmcnik, P. P. Lopes, N. M. Markovic, Energy and fuels from electrochemical interfaces. *Nat Mater* **16**, 57-69 (2016).
22. J. Suntivich, E. E. Perry, H. A. Gasteiger, Y. Shao-Horn, The Influence of the Cation on the Oxygen Reduction and Evolution Activities of Oxide Surfaces in Alkaline Electrolyte. *Electrocatalysis* **4**, 49-55 (2013).
23. M. Liu *et al.*, Enhanced electrocatalytic CO2 reduction via field-induced reagent concentration. *Nature* **537**, 382-386 (2016).
24. E. Perez-Gallent, G. Marcandalli, M. C. Figueiredo, F. Calle-Vallejo, M. T. M. Koper, Structure- and Potential-Dependent Cation Effects on CO Reduction at Copper Single-Crystal Electrodes. *J Am Chem Soc* **139**, 16412-16419 (2017).
25. A. S. Varela, W. Ju, T. Reier, P. Strasser, Tuning the Catalytic Activity and Selectivity of Cu for CO2 Electroreduction in the Presence of Halides. *Acs Catalysis* **6**, 2136-2144 (2016).
26. L. D. Chen, M. Urushihara, K. R. Chan, J. K. Norskov, Electric Field Effects in Electrochemical CO2 Reduction. *Acs Catalysis* **6**, 7133-7139 (2016).
27. J. Resasco *et al.*, Promoter Effects of Alkali Metal Cations on the Electrochemical Reduction of Carbon Dioxide. *J Am Chem Soc* **139**, 11277-11287 (2017).
28. B. Garlyyev, S. Xue, S. Watzele, D. Scieszka, A. S. Bandarenka, Influence of the Nature of the Alkali Metal Cations on the Electrical Double-Layer Capacitance of Model Pt(111) and Au(111) Electrodes. *J Phys Chem Lett* **9**, 1927-1930 (2018).
29. M. Valvo, S. Doubaji, I. Saadoune, K. Edström, Pseudocapacitive charge storage properties of Na2/3Co2/3Mn2/9Ni1/9O2 in Na-ion batteries. *Electrochimica Acta* **276**, 142-152 (2018).
30. V. Augustyn, P. Simon, B. Dunn, Pseudocapacitive oxide materials for high-rate electrochemical energy storage. *Energy & Environmental Science* **7**, 1597-1614 (2014).
31. X. Yu *et al.*, Emergent Pseudocapacitance of 2D Nanomaterials. *Advanced Energy Materials* **8**, (2018).
32. X. Q. Yang *et al.*, Temperature dependence of ion pairing of a potassium salt in nonaqueous liquid and polymer electrolytes: X-ray absorption studies. *The Journal of Chemical Physics* **101**, 3230-3233 (1994).
33. M. Harada, T. Okada, Hydration of counterions in cation exchange resins studied by X-ray absorption fine structure. *Chemical Communications*, 5182-5184 (2008).
34. D. Timothy *et al.*, *Hydration Structure of Sodium and Potassium Ions with DFT-MD*.

(2018).
35. R. Kortlever, J. Shen, K. J. Schouten, F. Calle-Vallejo, M. T. Koper, Catalysts and Reaction Pathways for the Electrochemical Reduction of Carbon Dioxide. *J Phys Chem Lett* **6**, 4073-4082 (2015).
36. K. Manthiram, Y. Surendranath, A. P. Alivisatos, Dendritic assembly of gold nanoparticles during fuel-forming electrocatalysis. *J Am Chem Soc* **136**, 7237-7240 (2014).
37. S. Ringe *et al.*, Understanding cation effects in electrochemical CO2 reduction. *Energy & Environmental Science*, (2019).
38. D. Gao *et al.*, Size-dependent electrocatalytic reduction of CO2 over Pd nanoparticles. *J Am Chem Soc* **137**, 4288-4291 (2015).

Acknowledgments: This work made use of the facilities at the NMR Facility, College of Chemistry, University of California, Berkeley. ICP-OES was supported by the Microanalytical Facility, College of Chemistry, University of California, Berkeley. We acknowledge Sirine Fakra for assistance with XAS experiments at the Beamline 10.3.2 at the Advanced Light Source. The authors also thank Tom Lin and Jan Chan for experimental assistance. **Funding:** This work was supported by Director, Office of Science, Office of Basic Energy Sciences, Chemical Sciences, Geosciences, & Biosciences Division, of the U.S. Department of Energy under contract no. DE-AC02-05CH11231, FWP CH030201 (Catalysis Research Program). Work at the Molecular Foundry was supported by the Director, Office of Science, Office of Basic Energy Sciences, of the U.S. Department of Energy under contract no. DE-AC02-05CH11231. This research used resources of the Advanced Light Source, which is a DOE Office of Science User Facility under contract no. DE-AC02-05CH11231. H.F. was supported by the Director, Office of Science, Office of Basic Energy Sciences, Division of Chemical, Geological and Biosciences of the US Department of Energy under contract No. DE-AC02-CH11231 (Solar Photochemistry Research Program). D.K. and S.Y. acknowledge support from Samsung Scholarship. **Author contributions:** D.K. and S.Y. designed and performed experiments, and analyzed data with assistance from Y.L. and S.L. F.Z. conducted molecular dynamics simulation under the supervision of L.W. H.F. assisted infrared spectroscopy measurements. P.Y. supervised the project and experimental design. All authors wrote the manuscript. **Competing interests:** Authors declare no competing interests. **Data and materials availability:** All data is available in the main text or the supplementary materials.

Supplementary Materials:

Materials and Methods

Supplementary Text

Figures S1-S32

Tables S1

References